48th AIAA Aerospace Sciences Meeting Including the New Horizons Forum and Aerospace Exposition
4 - 7 January 2010, Orlando, Florida

AIAA 2010-389

Effect of Aspect Ratio on Rigid Lifting Flat Plates in Pitch-Plunge Motion at Low Reynolds Numbers

Jonathan M. Rausch[1]*, Yeon Sik Baik[2]*, Luis P. Bernal[3]* and Michael V. Ol[4]**

University of Michigan, Ann Arbor, MI, 48109

**U.S. Air Force Research Laboratory, Wright-Patterson Air Force Base, OH 45433, U.S.A.*

Flowfield behavior of wall-to-wall and low aspect ratio (AR=2) rigid flat plates in pitching and plunging motion is studied in a water tunnel at low Reynolds numbers. All models have a 152mm chord and t/c = 2.25%. Two sets of kinematics already well-established in the recent literature are used: combined pitch and plunge, where pitch angle of attack partially cancels plunge-induced angle of attack, and pure plunge. Three Reynolds numbers ($1x10^4$, $3x10^4$, and $6x10^4$) are considered, using dye flow visualization and particle image velocimetry (PIV). Broadly, sectional vorticity contour plots reveal similarity between the nominally 2D and AR=2 plates, but there are several interesting exceptions. The AR=2 plate exhibited a marked axial flow when the effective angle of attack was near its maximum. For the pitching and plunging motion the AR=2 plate showed open separation at phase of 180°, while the nominally two-dimensional model has closed separation throughout the downstroke. For validation of the PIV results, a comparison is made between Reynolds number $3x10^4$ and $4x10^4$ three-dimensional models at the University of Michigan and Air Force Research Laboratory (AFRL), respectively.

Nomenclature

c	chord [m]
f	frequency [Hz]
h_o	reduced plunge amplitude of oscillation
k	reduced pitch frequency, $k = \pi f c / U_\infty$
L	length [m]
Re	Reynolds number, $Re = c U_\infty / \nu$
St	Strouhal number, $St = 2 f h_o / U_\infty = 2 k h_o / \pi$
t	time [s]
t/c	thickness-to-chord ratio [%]
$\bar{u}$	mean x-component of velocity vector [m/s]
$\overline{u'}$	mean fluctuation of x-component of velocity vector [m/s]
$\overline{u'v'}$	Reynolds stress [m²/s²]
U_∞	freestream velocity [m/s]
$\bar{v}$	mean y-component of velocity vector [m/s]
$\overline{v'}$	mean fluctuation of y-component of velocity vector [m/s]
x	Cartesian x-coordinate [m]
$\frac{x}{c}$	chord normalized x-coordinate

---

[1] Graduate Research Assistant, University of Michigan, Department of Aerospace Engineering
[2] Graduate Research Assistant, University of Michigan, Department of Aerospace Engineering
[3] Associate Professor, University of Michigan, Department of Aerospace Engineering, lpb@umich.edu.
[4] Aerospace Engineer, Air Vehicles Directorate, Wright-Patterson AFB

y	Cartesian y-coordinate [m]
$\frac{y}{c}$	chord normalized y-coordinate

Greek Symbols

α_{eff}	effective angle of attack [deg.]
α_0	mean angle of attack [deg.]
λ	ratio of pitch amplitude to plunge induced angle of attack amplitude
ν	kinematic viscosity [m^2/s]
ϕ	positive phase offset for pitch relative to plunge [rad.] or phase of motion [deg.]
ω^*	normalized vorticity, $\omega^* = \omega c / U_\infty$

I. Introduction

We continue our series of water tunnel experiments on the flowfields of pitching and plunging rigid foils and plates, now with extension to low aspect ratio planforms. The motivating application continues to be Micro Air Vehicles (MAVs) [1] and the resulting low Reynolds numbers (10^4-10^5). The roles of flow separation and large scale vortical structures in flapping wing flight are of particular interest. The kinematics of flapping wing flight involve large amplitude oscillations of pitch and plunge. The presence of flow separation and large scale vortical structures has notional parallels to dynamic stall[2] phenomena generally associated with helicopter blade research[3]. Dynamic stall is the formation, separation, and convection of a leading edge vortex that produces a transient chordwise pressure distribution significantly different from static stall. In addition to the physics associated with dynamic stall phenomena, the role of laminar-to-turbulent transition in flapping wing flight remains of significance, since transition can significantly affect the nature of flow separation and thus the aerodynamic loads time history[4].

Here we extend recent work on wall-to-wall or nominally 2D pitching/plunging plates to low aspect ratio. Baik, et al.[4] examined the effect of Reynolds number and airfoil shape for nominally two-dimensional models. We retain the same kinematics, but generalize to an AR=2 plate, and consider second-order flowfield statistics for the 2D and low-AR case in detail.

II. Experimental Setup

The University of Michigan's closed loop, free surface water tunnel has test section of 61 x 61 cm with glass sides and bottom, freestream velocity range from 5 cm/s to 40 cm/s, and turbulence intensity of 1.15% (measured using particle image velocimetry, and including low-frequency bulk-flow undulations).

Models are actuated by a pitch-plunge oscillator rig above the tunnel's free surface, consisting of a B4872TS Rotary Table (for pitch) and a Velmex 20-inch BiSlide (for plunge). Both motors are controlled by a Velmex VXM-1-1 motor controller. Models are suspended vertically from the pitch-plunge oscillator rig. Both models were stainless steel with a $t/c = 2.25\%$ and $c = 152$mm. For clarification the two flat plate models will be referred to as the "2D model" for the model spanning the test section and the "3D model" for the AR=2 model. The 3D model is an AR=1 semi-span with an endplate used as a symmetry plane. The surfaces of the stainless steel flat plates were polished for a specular reflection of PIV laser light.

Dye injection was used for qualitative flow visualization and to predicatively arrange the PIV. Dye is introduced by a seven-prong rake upstream of the model at the midspan for the 2D plate and at the 3/4-span for the 3D plate, and is driven by a positive-displacement infusion pump to maintain efflux speed matching with the free-stream. The resulting streaklines produce a global portrait of flow separation and if interpreted with care, are a useful surrogate for tagging vortical structures. Spanwise locations of dye injection also correspond to the PIV measurement planes.

Two camera views were used to capture the flow visualization. One was perpendicular to plane of the injected dye flow and is thus coincident with PIV. The other was normal to the free-stream, to capture spanwise flow.

A. Particle Image Velocimetry

The PIV system is double frame, single exposure, using a Quanta-Ray PIV Series Pulsed Nd:YAG laser and two Cooke Corporation PCO.4000, 4008 x 2672 pixel CCD cameras. Both cameras used Nikon 105 mm lenses. Figure 1a depicts the orientation of the laser light sheet and camera relative to the test section of the water channel. Figure 1b is dye flow visualization image for the 3D model. In the image the coincident PIV/dye-flow plane is marked at the 3/4-span location with the green line; additionally, the end plate is observed at the top of Figure 1b. Table 1 recites the various PIV operational parameters.

Top View

Flow Direction

Light Sheet

Flat Plate Model

Side View

Flow Direction

Camera

(a)

End Plate

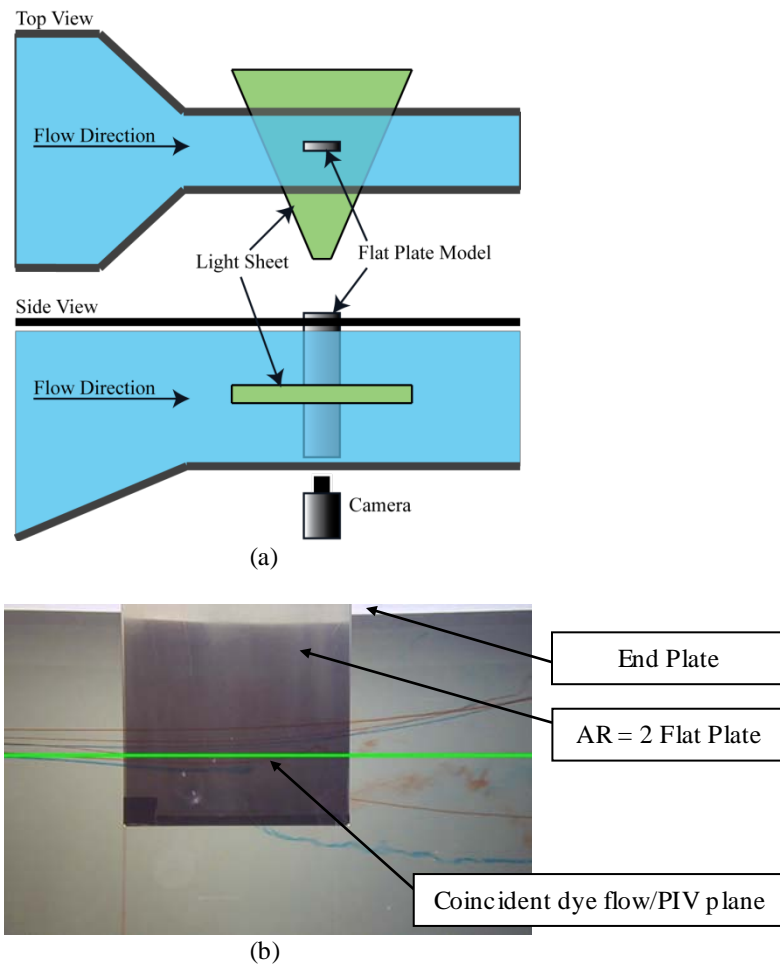AR = 2 Flat Plate

Coincident dye flow/PIV plane

(b)

Figure 1. Diagram of the PIV setup with respect to the water channel's test section. The diagram is an example of the two-dimensional flat plate setup with the model spanning the entire depth of the test section.

Table 1. Table of PIV parameters for the two- and three-dimensional flat plates

Model	
Chord, c [mm]	152 (for 2D and 3D models)
t/c ratio [%]	2.25
3D flat plate length [mm]	152
Flow	
Fluid	Water
Re	1×10^4, 3×10^4, and 6×10^4
U_∞ [cm/s]	6.6, 19.7, and 39.5 (in order of increasing Re)
Seeding	
Type	TiO_2
Particle Physical Diameter [μm]	3
Dispersant	DARVAN C-N
Laser	
Type	Nd:YAG
Max Pulse Energy [mJ/pulse]	200
Recording	
approx. FOV [mm^2]	20,000
Camera	PCO.4000
Pixel Length Scale [pixels/mm]	25
Dynamic Range	16 bit
f-number	5
Focal length [mm]	105
Particle Image Diameter [pixels]	3
Δt [ms]	4.82, 1.60, and 0.80 (in order of increasing Re)
Image Pair Processing	
High Resolution Window [pixels^2]	32 x 32
Low Resolution Window [pixels^2]	64 x 64
Sample Size* [min. - max.]	approx. 175 – 200
Total DPIV Realizations	200

* Sample size refers to the number of independent samples that remain after bad data points are replaced using a median filter, the sample size is given as a range from smallest to largest throughout the data.

B. Air Force Research Laboratory Experiments

Experiments performed in the AFRL Horizontal Free-surface Water Tunnel (HFWT) on a very similar flow configuration are also reported here. The HFWT has a 46 cm wide by 61cm deep test section with glass sides and bottom, freestream velocity range from 3 cm/s to 45 cm/s, and turbulence intensity of 0.5%. The each plunge rod is attached to a linear servomotor oriented vertically above the test section of the HFWT. For a more detailed discussion of the experimental facility and PIV procedure consult Ol, *et al.*[2]

In contrast to the model mounting scheme used at the University of Michigan, the AFRL model is a full span model mounted on a sting attached to the model's trailing edge at the midspan. The moutning scheme is depicted in Figure 2.
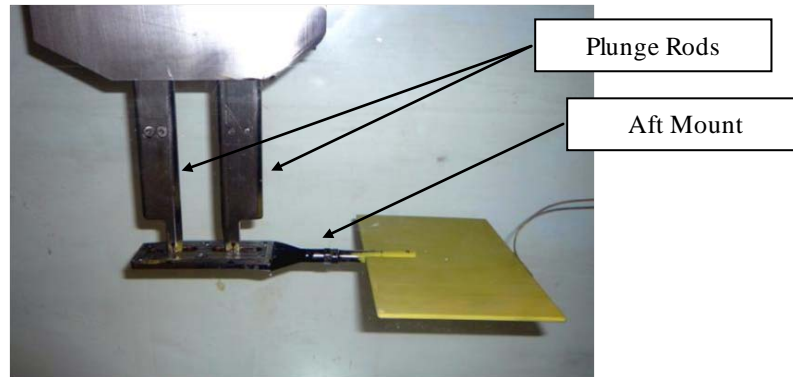

Figure 2. AFRL aft sting mount

American Institute of Aeronautics and Astronautics

In the AFRL experiments the kinematic scaling parameters are the same as the University of Michigan (UM) experiments except for the Reynolds number. The AFRL data has Reynolds number 40,000 while the UM data has Reynolds number 30,000.

III. Results

The two model kinematics are a pitch--plunge and pure plunge. For both, the effective angle of attack time history is given by Equation 1.

$$\alpha_{eff} = \alpha_0 + \lambda \arctan(\pi\, St)\cos\{2\pi(ft + \phi)\} + arctan\{\pi St\, \sin(2\pi ft)\} \qquad (1)$$

Both sets of kinematics use a Strouhal number equal to 0.08, a reduced pitching frequency of $k = 0.25$, and a mean angle of attack of $8°$. For the pitch-plunge motion the plunge component lags the pitch component by a quarter of the period and the ratio of pitch amplitude to plunge induced angle of attack, λ, is 0.6. The λ parameter governs how much pitch reduces the plunge-induced effective angle of attack. For pure plunge, $\lambda = 0$. The effective angle of attack history is plotted in Figure 3.
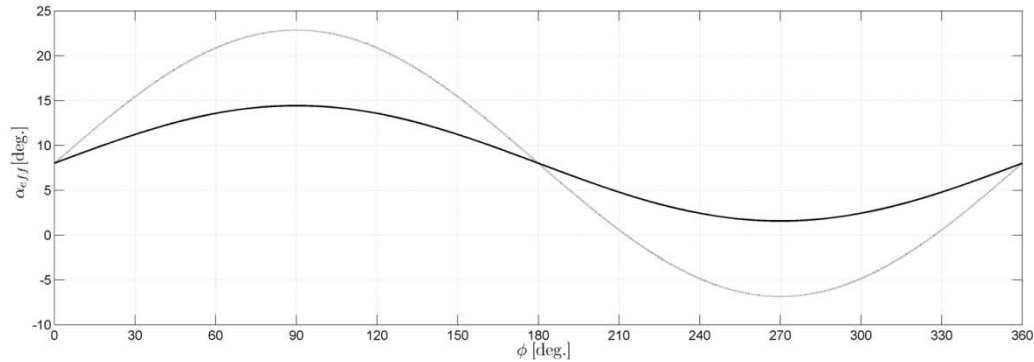
Figure 3. Effective angle of attack time histories for pitch-plunge (solid line) and plunge (dotted line).

The pitch-plunge was motivated by the desire for kinematics that maximize propulsive efficiency[5]. The pitch-plunge kinematics were designed for a SD7003 airfoil and the effective angle of attack would make small excursions in effective angle of attack past the SD7003's static stall angle of attack. Therefore, for the SD7003 the pitch-plunge kinematics would result in relatively weak dynamic stall. The pure-plunge was simply an attempt to explore deep dynamic stall. Both have been examined in detail for 2D models[4,6]. Ol, *et al.*[2] considered the SD7003 airfoil in combined experiment and computation at Re = 60K, comparing lift history with Theodorsen's formula for attached flow and planar wakes. The pitch-plunge evinced a trailing edge separation throughout the motion's downstroke and the plunge kinematics resulted in a leading edge separation and a pronounced leading and trailing edge vortex. Kang, *et al.*[6] generalized these results to the Re range of 1×10^4 to 6×10^4, and Baik, *et al.*[4] compared the SD7003 airfoil to a 2D, finding that the plate produced stronger leading-edge separation but less Reynolds number dependency.

The present study uses one of the previously studied Reynolds numbers (relying on the Re-independence found in Baik, *et al*[4]) and both sets of motion kinematics. An additional 2D flat plate experiment was performed at the same Re as the 3D flat plate in pure-plunge.

Table 2 lists test conditions and motion phases at which PIV snapshots were taken for the 2D plate, and Table 2 does the same for the 3D plate.

American Institute of Aeronautics and Astronautics

Table 2. The 2D flat plate dye flow and PIV test matrix for the five sets of Reynolds number and kinematics

Experiment ID	Re	Kinematics	ϕ	Realizations per Phase
1[4]	10,000	Pitch-Plunge	$0°, 90°, 120°, 150°, 180°, 270°$	204
2[4]	30,000	Pitch-Plunge	$0°, 90°, 120°, 150°, 180°, 270°$	204
3[*]	30,000	Plunge	$0°, 90°, 120°, 150°, 180°, 270°$	200
4[4]	60,000	Pitch-Plunge	$0°, 90°, 120°, 150°, 180°, 270°$	200
5[4]	60,000	Plunge	$0°, 90°, 120°, 150°, 180°, 270°$	200

[*] *Two-dimensional flat plate experiment not performed in Baik, et al[4].*

Table 3. The 3D flat plate dye flow and DPIV test matrix

Experiment ID	Re	Kinematics	ϕ	Realizations per Phase
6	30,000	Pitch-Plunge	$0°, 90°, 120°, 150°, 180°, 270°$	200
7	30,000	Plunge	$0°, 90°, 120°, 150°, 180°, 270°$	200

Results for $\phi = 270°$ (halfway through the upstroke; effective angle of attack $(\alpha_{eff})_{\phi=270°} = 1.6°$ for pitch-plunge and $(\alpha_{eff})_{\phi=270°} = -6.85°$ for plunge) is deemphasized, as the flow is mostly attached.

A. Two-Dimensional Model: Pitching and Plunging Motion (Baik, *et al[4].*)

2D pitch-plunge at Re = 30,000 was presented in Baik, *et al[4]*. and is reproduced here to compare with the 3D plate. The flow visualization and PIV data is presented in Figure 4 and Figure 5, respectively. Figure 4 presents a comparison of flow visualization, $\bar{u}$, and ω^* for the pitching and plunging flat plate. Figure 5 presents the phase-averaged second-order turbulence statistics.

The pitching and plunging two-dimensional model begins the motion at $\phi = 0°$ with transitional vortical-structures that are phase-locked near the leading edge. From approximately the half-chord location to the trailing edge the flow is attached. From $\phi = 90° - 180°$ a region of growing closed separation forms over the entire chord. The region of closed separation is bounded by a turbulent shear layer that has negative $\overline{u'v'}/U_\infty^2$. Anisotropy is observed in the velocity correlations with $\overline{u'^2}$ more prevalent than $\overline{v'^2}$.
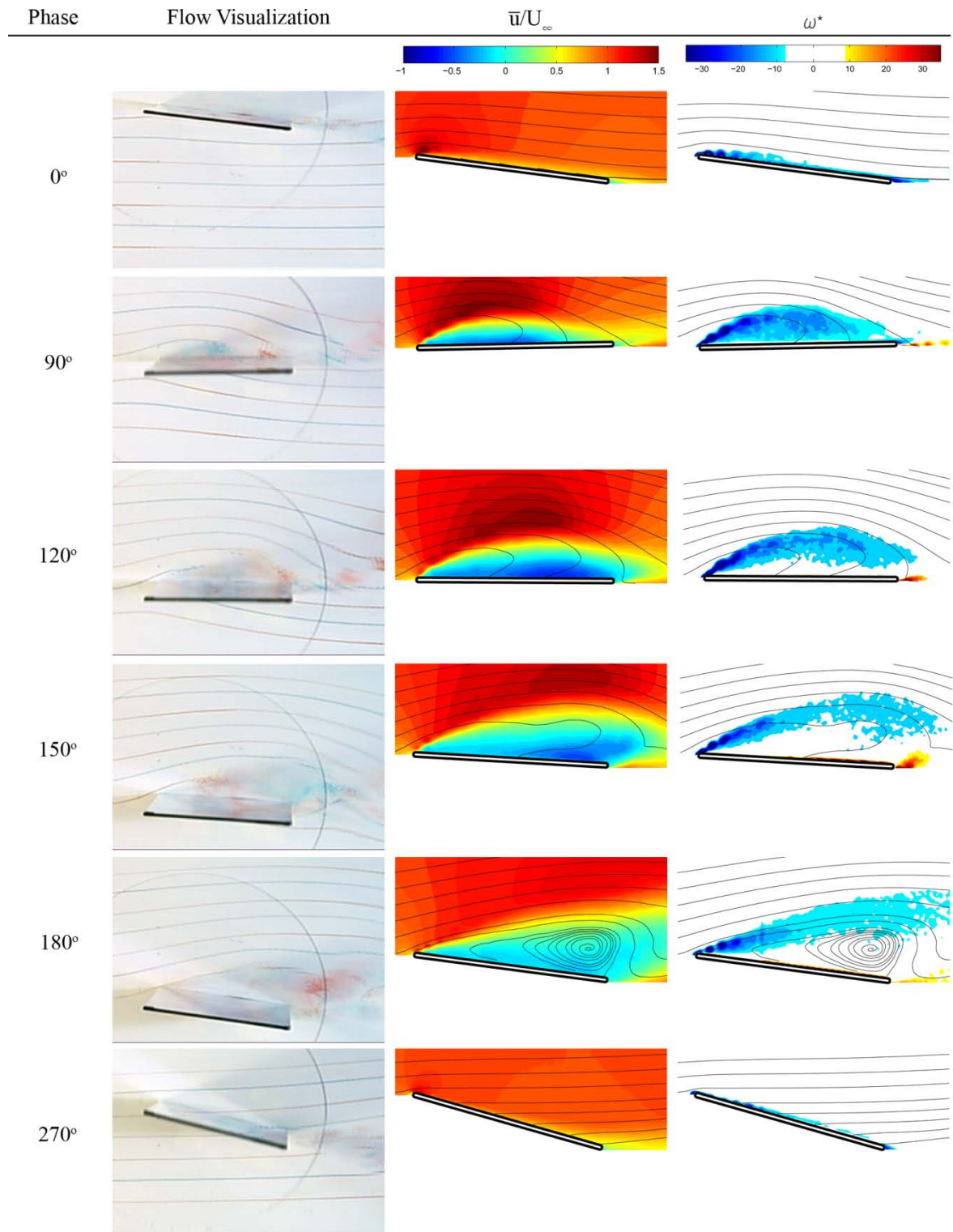
Phase	Flow Visualization	$\overline{u}/U_\infty$	ω^*

Figure 4. Flow visualization, $\overline{u}$, and ω^* for the pitching and plunging 2D flat plate at Re = 30,000

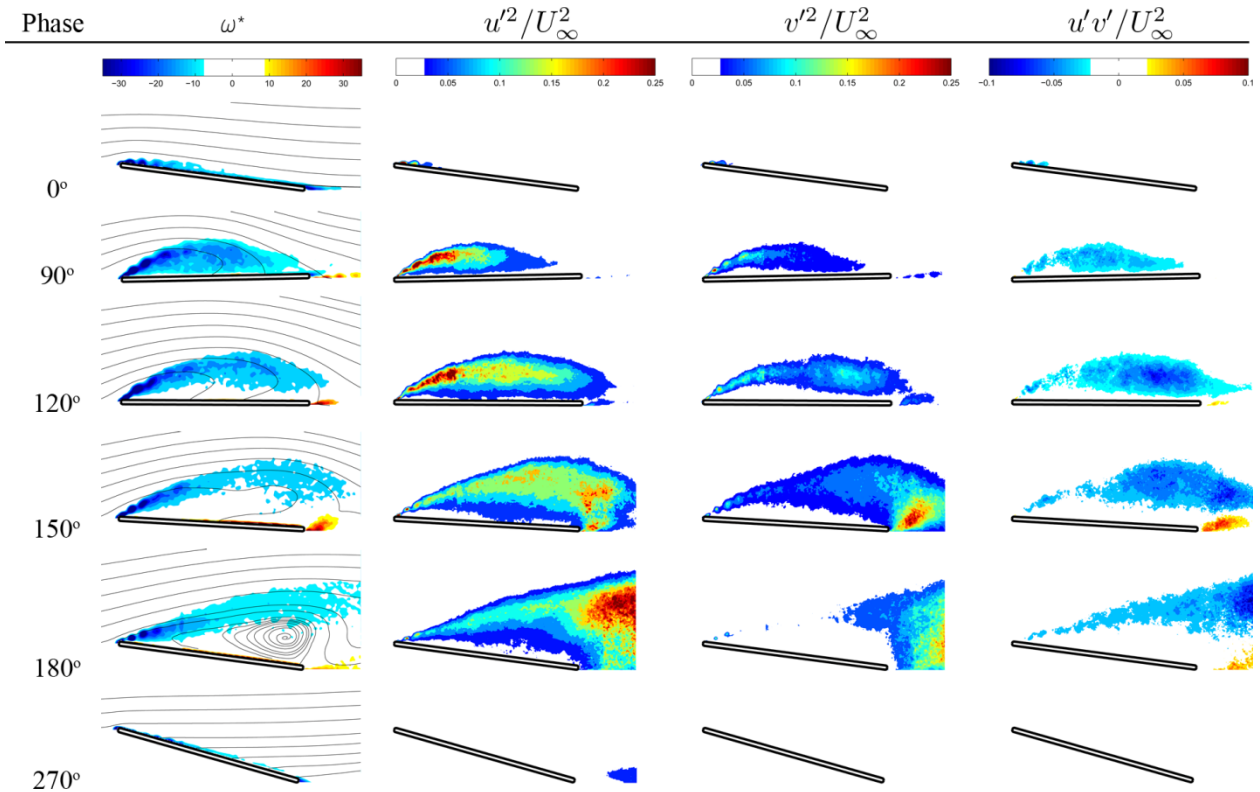American Institute of Aeronautics and Astronautics

Figure 5. Second order turbulence statistics for the pitching and plunging 2D flat plate at Re = 30,000

B. Two-Dimensional Model: Plunging Motion

Pure-plunge 2D flat plate data are shown in Figure 6 (dye flow visualization, $\bar{u}$, and ω^*) and Figure 7 (vorticity and second-order phase-averaged turbulence statistics).

For the plunging 2D flat plate the dramatic changes in flow topology can be attributed to the large effective angle of attack. The dominant characteristic of the flowfield is the formation of large leading and trailing edge vortices. At $\phi = 0°$ the vorticity field shows a small region of leading edge separation with phase-locked transitional vortical-structures (confirmed by the turbulence statistics in Figure 7). The leading edge separation then grows to a large leading edge vortex by $\phi = 90°$. The leading edge vortex has negative $\overline{u'v'}/U_\infty^2$ values along with $\overline{u'^2}/U_\infty^2$ and $\overline{v'^2}/U_\infty^2$ of equal magnitude. The turbulence statistics suggest that the turbulent flow in the leading edge vortex is isotropic. For the leading edge vortex, turbulence statistics associated with phase-locked vortical-structures can be the result of cycle-to-cycle variation in the location of vortices. The leading edge vortex convects downstream where it interacts with the trailing edge vortex at $\phi = 120°$. The turbulence statistics are isotropic with negative and positive $\overline{u'v'}/U_\infty^2$. The negative $\overline{u'v'}/U_\infty^2$ is associated with the shed leading edge vortex and a region of positive vorticity created by the interaction of the leading edge vortex with surface of the flat plate. The positive $\overline{u'v'}/U_\infty^2$ is associated with the growing trailing edge vortex. By $\phi = 150°$ the leading edge vortex has left the PIV field-of-view and the trailing edge vortex is convecting downstream. At $\phi = 180°$ the leading and trailing edge vortices have left the PIV field-of-view and one finds open separation. The turbulence statistics of the last two phases of the downstroke evince isotropic turbulence in the leading edge shear layer that bounds the flow separation.
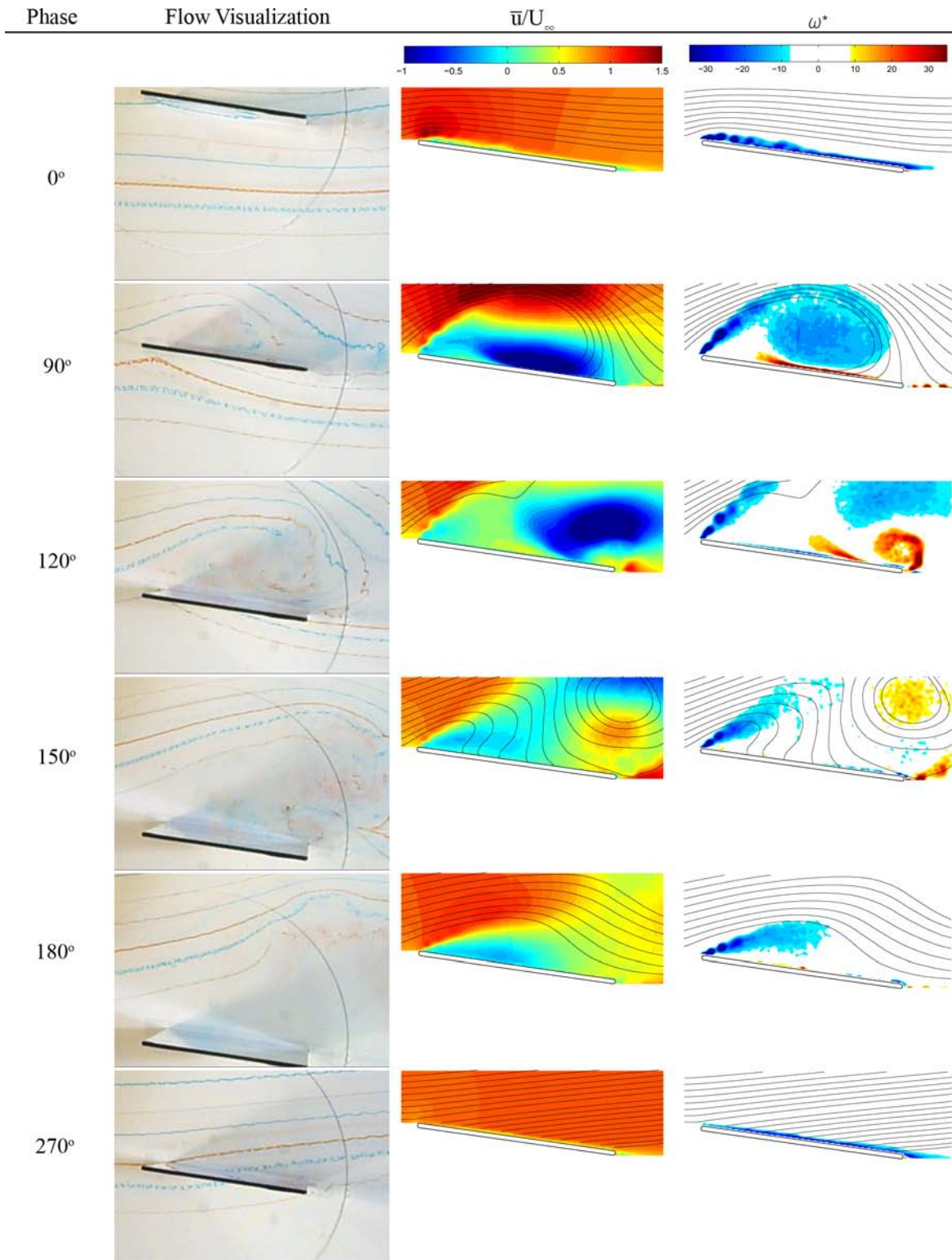
American Institute of Aeronautics and Astronautics

Figure 6. Flow visualization, $\overline{u}$, and ω^* for the plunging two-dimensional flat plate at Re = 30,000

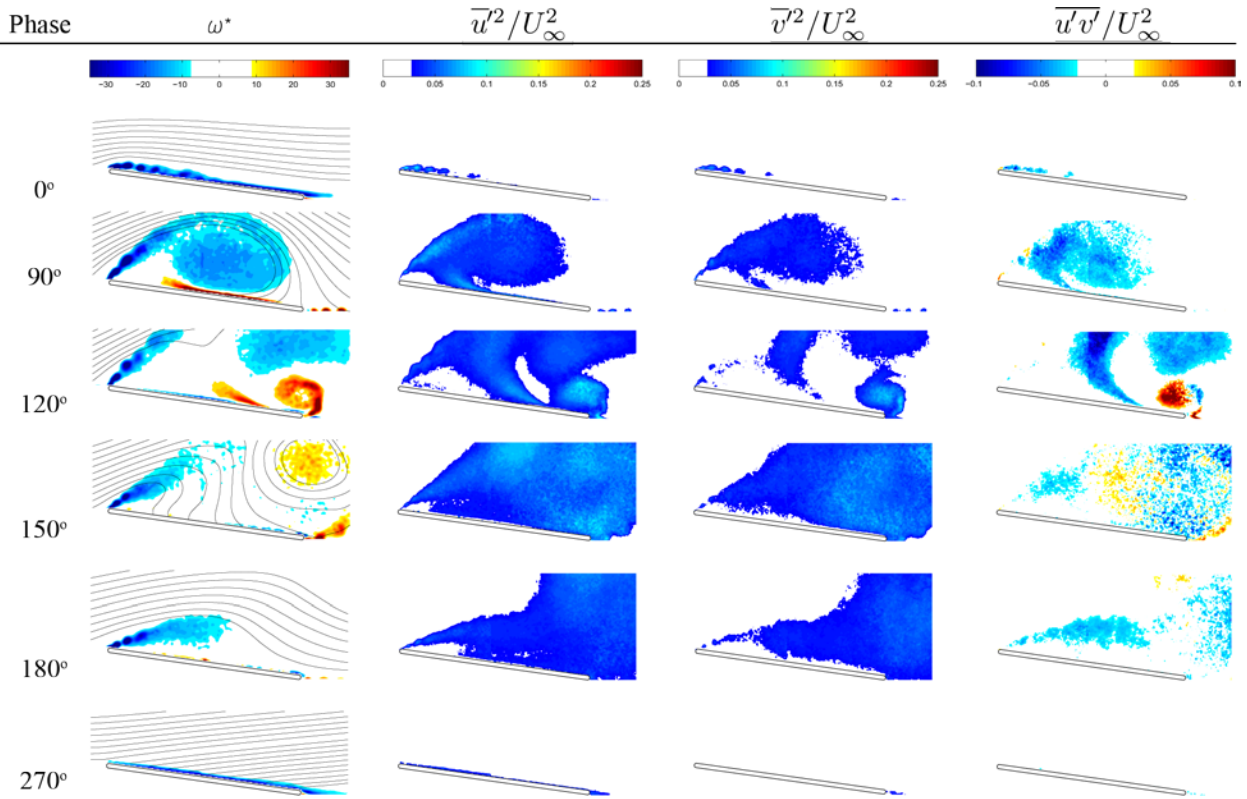American Institute of Aeronautics and Astronautics

Figure 7. Second order turbulence statistics for the plunging 2D flat plate at Re = 30,000

C. Three-Dimensional Model: Pitching and Plunging Motion

Pitching-plunging 3D plate results are given in Figure 8 (dye flow visualization, $\bar{u}$, and ω^*) and Figure 9 (vorticity with the second order turbulence statistics) for the plunging flat plate. Figure 9 compares the.

Similar to the 2D model results at $\phi = 0°$, phase-locked transitional vortical-structures are observed near the leading edge. These promote reattachment. The most notable observation of the pitching and plunging 3D flat plate is the region of closed separation that occurs from $\phi = 90° - 150°$. In Figure 8 at $\phi = 90°$ the location and size of this closed leading edge separation do not significantly change as the flow temporally evolves. Independent of model motion or Reynolds number, for the 3D flat plate a region of closed leading edge separation is present at $\phi = 90°$ that affects the flow over the entire chord as the flow reattachment point moves toward the trailing edge. The growth of the closed leading edge separation is not present for the three-dimensional flat plate. Examination of the streamlines in Figure 8 shows a region of closed separation with the same approximate spatial extent from $\phi = 90° - 150°$. Examination of the turbulence statistics during these phases yields negative $\overline{u'v'}/U_\infty^2$ for the closed separation's bounding shear layer.
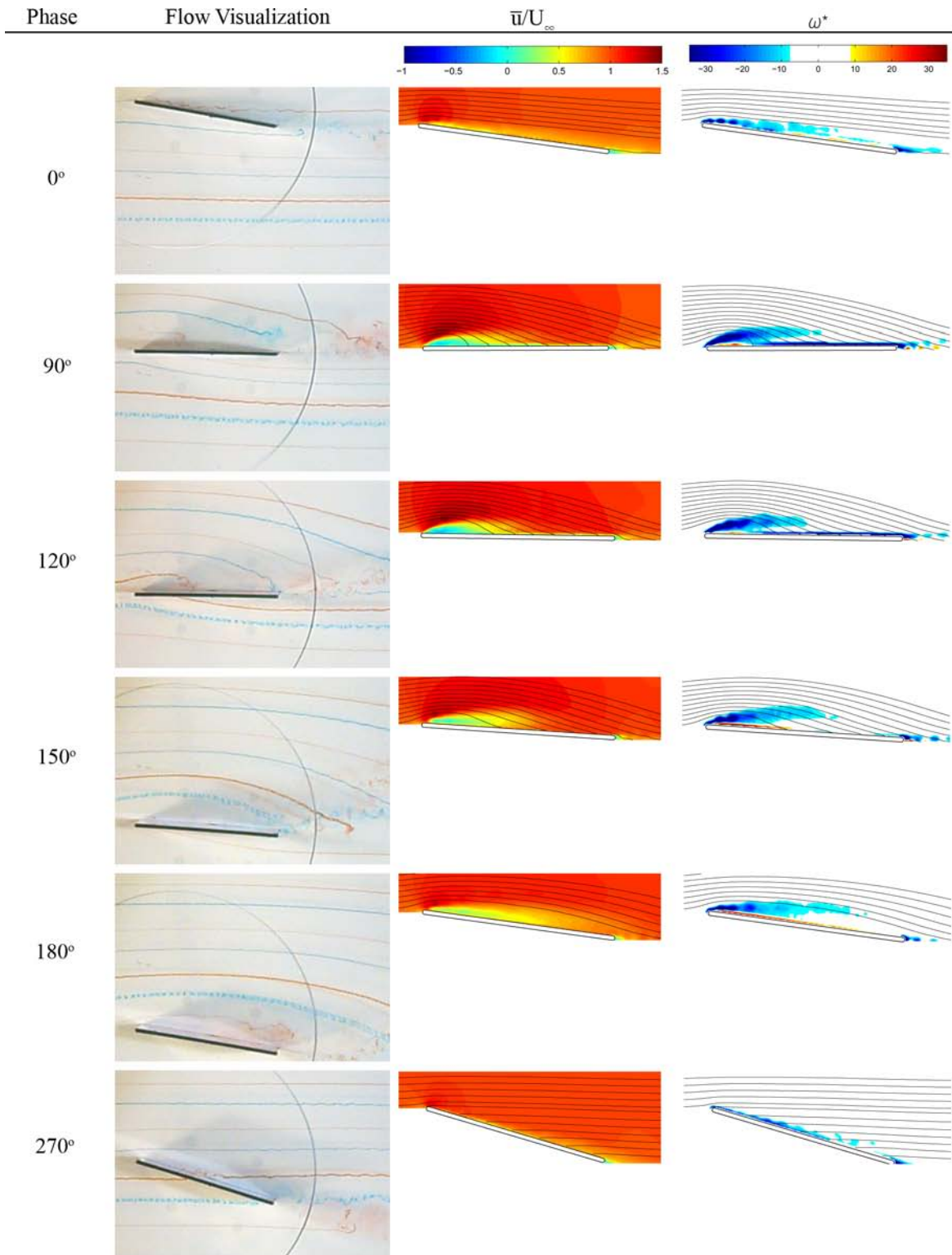
American Institute of Aeronautics and Astronautics

Phase	Flow Visualization	$\overline{u}/U_\infty$	ω^*
0°			
90°			
120°			
150°			
180°			
270°			

Figure 8. Flow visualization, $\overline{u}$, and ω^* for the pitching and plunging 3D flat plate at Re = 30,000

American Institute of Aeronautics and Astronautics
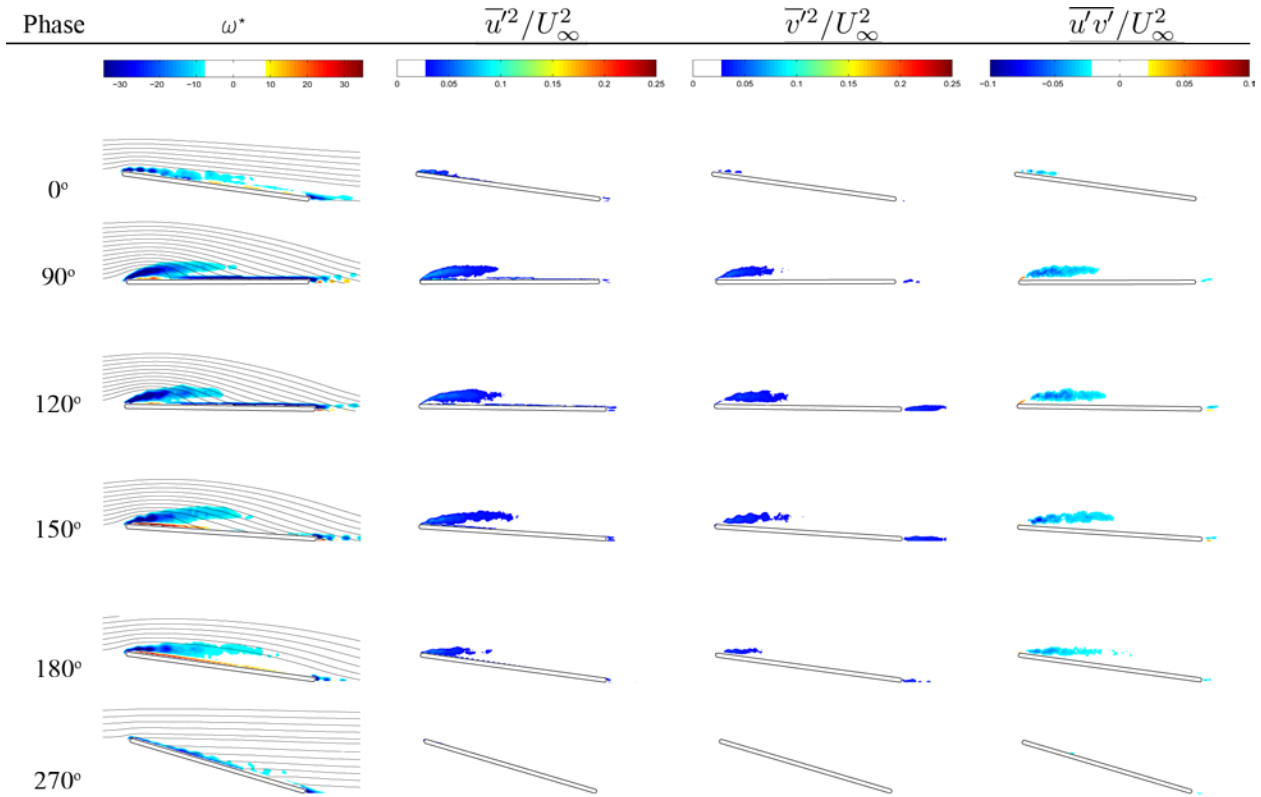
Figure 9. Turbulence statistics for the pitching and plunging 3D plate at Reynolds number 30,000.

D. Three-Dimensional Model: Plunging Motion

Pure-plunge 3D flat plate results are presented in Figure 10 (dye flow visualization, $\bar{u}$, and ω^*) and Figure 11 (vorticity with the second order turbulence statistics).

Again, at $\phi = 0°$ phase-locked transitional vortical-structures are observed near the leading edge that promote reattachment. Similar to the pitching and plunging 3D flat plate, the most notable observation of the plunging 3D flat plate is the region of closed separation that occurs from $\phi = 90° - 150°$. The dynamics of the closed separation region are interesting when compared to the large leading and trailing edge vortices generated under the same experimental conditions for the 2D flat plate. In Figure 10 the location and size of this closed separation at $\phi = 90°$ does not significantly change as the flow temporally evolves. Examining the 2D flat plate under the same experimental conditions at $\phi = 90°$ yields the observation of a large leading edge vortex. At $\phi = 90°$ the large leading edge vortex affects the flow over the entire chord with the attaching near the trailing edge. The separation for the 2D flat plate is in stark contrast with the 3D flat plate. Examination of the streamlines shows a region of closed separation with the same approximate spatial extent from $\phi = 90° - 150°$. Examination of the turbulence statistics during these phases yields negative $\overline{u'v'}/U_\infty^2$ for the closed separation's bounding shear layer.
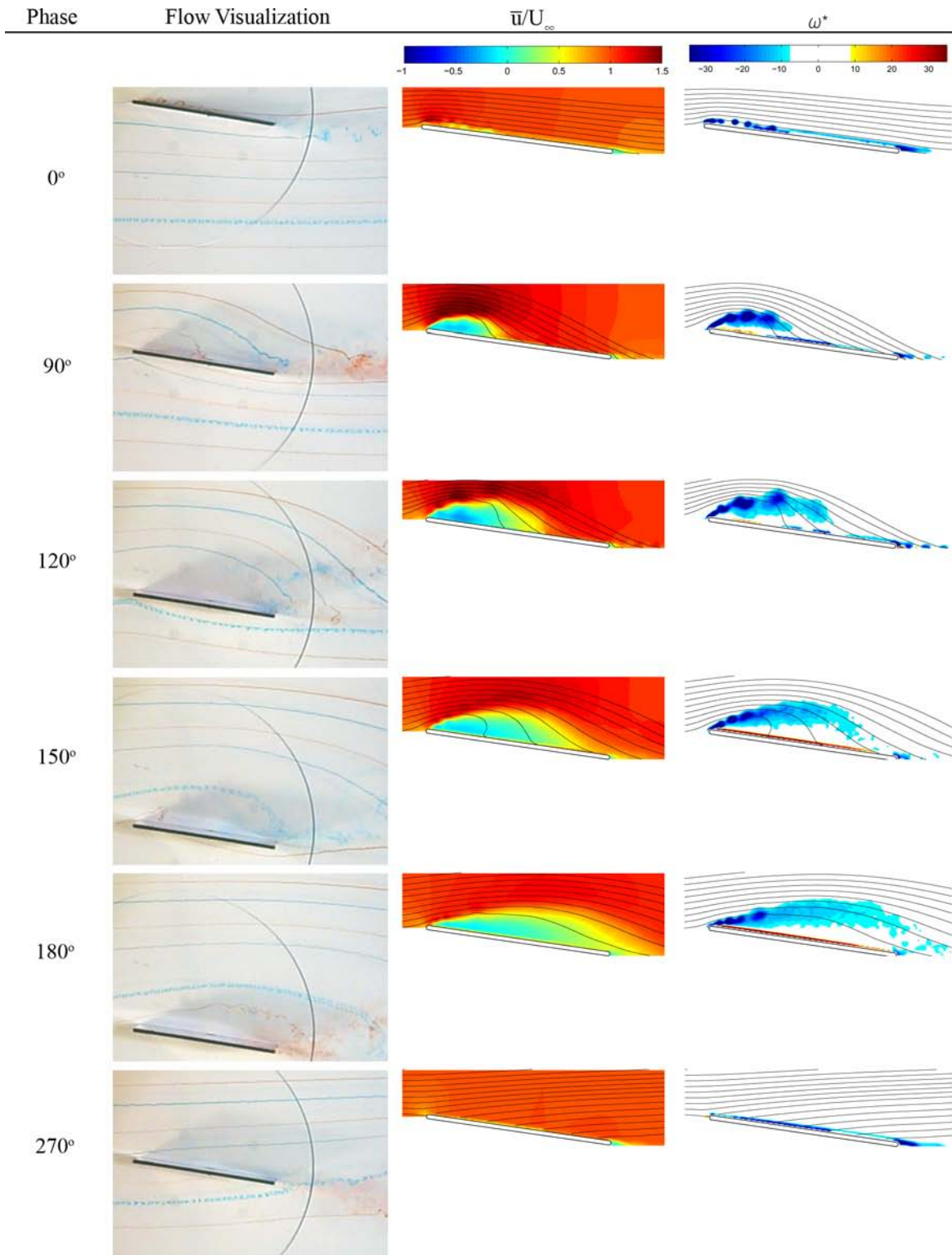
American Institute of Aeronautics and Astronautics

Figure 10. Flow visualization, $\overline{u}$, and ω^* for the plunging 3D flat plate at Re = 30,000
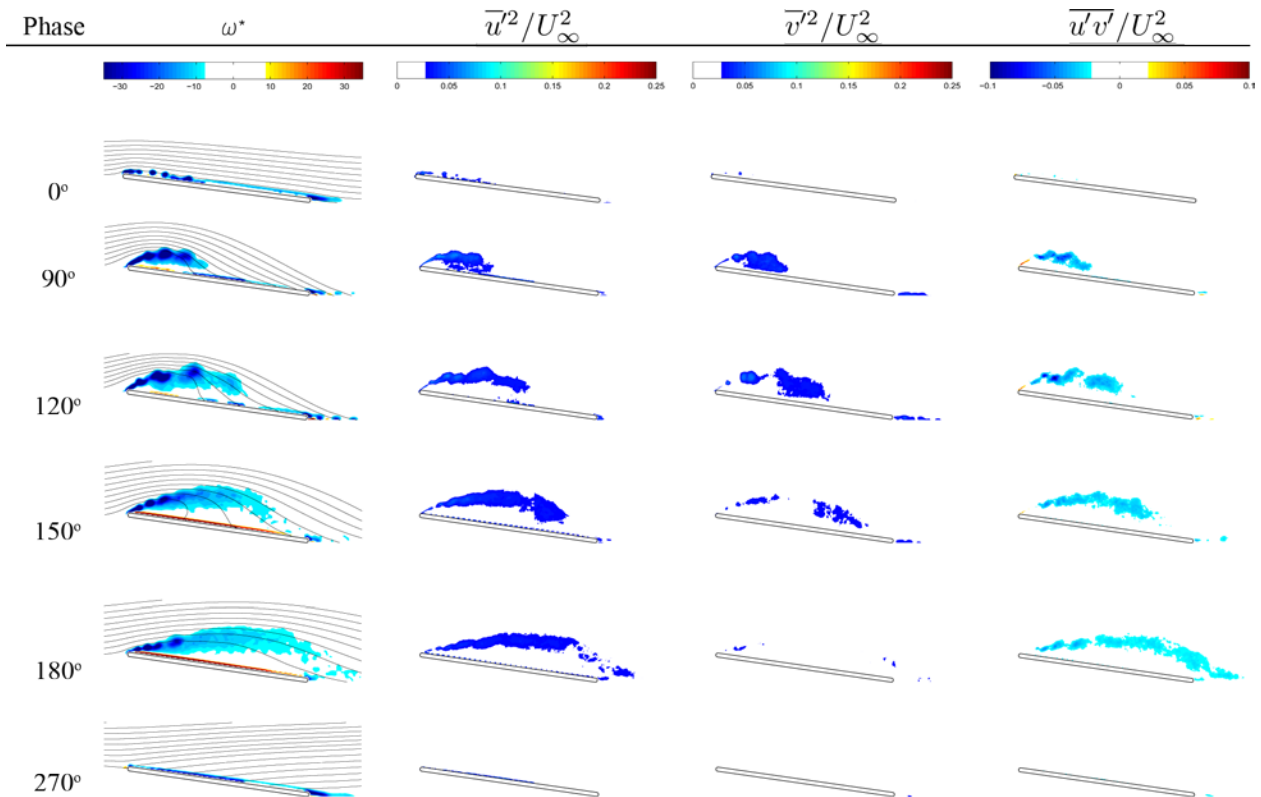
Figure 11. Turbulence statistics for the pure plunging 3D plate at Re = 30,000.

E. Three-Dimensional Model: University of Michigan and AFRL Comparison

Using the same kinematic parameters as the 3D flat plate for the UM PIV at Reynolds number 30,000, experimental validation was provided by the AFRL HFWT using an AR = 2 flat plate at the same Reynolds number. The normalized ū and vorticity fields comparing the AFRL and UM experiments are plotted in Figure 12 and Figure 13, the former figure compares pitching and plunging while the latter figure compares plunging.

The contours of normalized ū and vorticity in Figure 12 show qualitative agreement between the AFRL and UM with the main discrepancy being the chordwise extent of the flow separation. As previously observed in the UM PIV the separation that occurs at the leading edge is closed and the majority of the flow over the chord is attached through the downstroke. The AFRL separation at $\phi = 90° - 180°$ behaves similarly except that the separation consistently occupies larger fractions of the chord.

At $\phi = 0°$ both pitching and plunging PIV data sets have vortical structures in the leading edge shear layer. At subsequent phases the vortical instabilities are only present in the UM PIV.

The contours of normalized ū and vorticity in Figure 13 shows qualitative agreement between the AFRL and UM. Again the main discrepancy between the data sets is the chordwise extent of the flow separation. The separation through $\phi = 90° - 180°$ is comparable but the AFRL separation consistently occupies larger fractions of the chord.

At all phases of the downstroke the UM plunging PIV data has vortical structures in the leading edge shear layer. The AFRL plunging PIV never has this property throughout the motion.
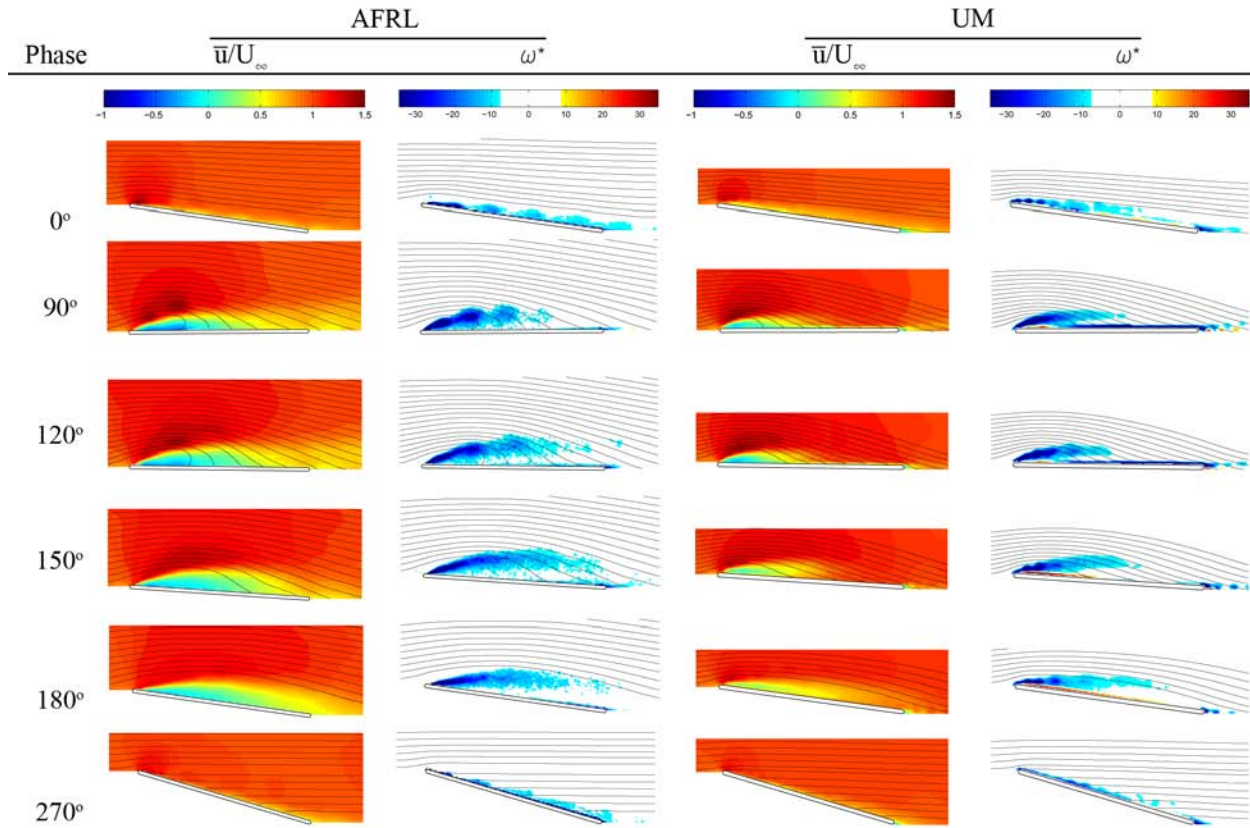
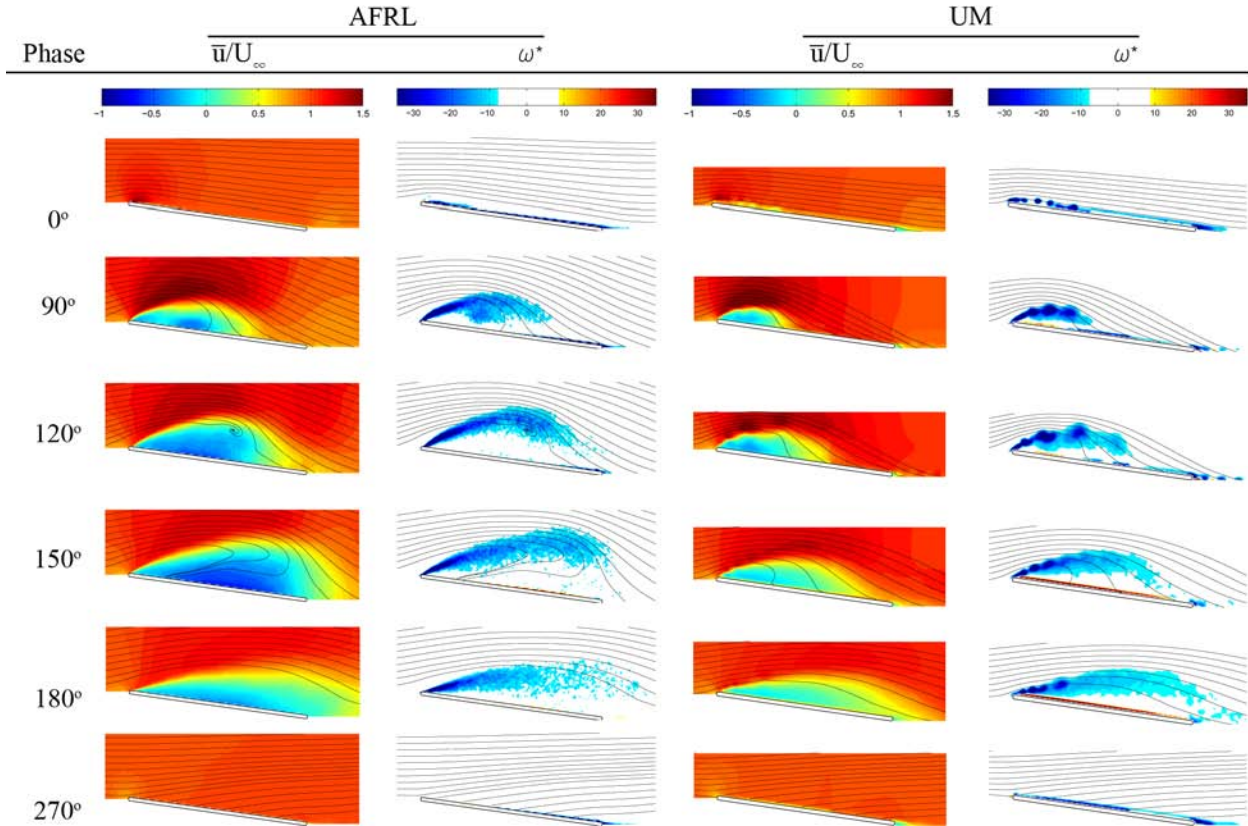***Figure 12.*** **ū and ω* for the pitching and plunging 3D flat plate at Re = 30,000 (AFRL/UM comparison)**

Figure 13.ū and ω* for the plunging 3D flat plate at Re = 30,000 (AFRL/UM comparison)

Distributions of normalized ū were plotted at chordwise locations to quantify the difference between the AFRL and UM PIV. Since the qualitative differences between data sets were observed in Figure 12 and Figure 13 from $\phi = 90° - 180°$, these phases were used to plot distributions of normalized ū in Figure 14 (pitch-plunge comparison) and Figure 15 (plunge comparison).

For the comparison of the pitching and plunging 3D flat plates in Figure 14 the AFRL separation affects a larger portion of the chord than the UM separation. This effect is best illustrated at the 50 and 75% chord locations where the AFRL normalized ū distribution is consistently more negative than the UM. However, the AFRL and UM data both have closed separation through the downstroke.

For the comparison of the plunging 3D flat plate in Figure 15 the AFRL separation has much stronger effect on the normalized ū distribution and it consistently occupies larger fractions of the chord. Both data sets have closed separation through $\phi = 90° - 150°$. At $\phi = 180°$ the AFRL data evinces open separation while the UM data evinces closed separation.
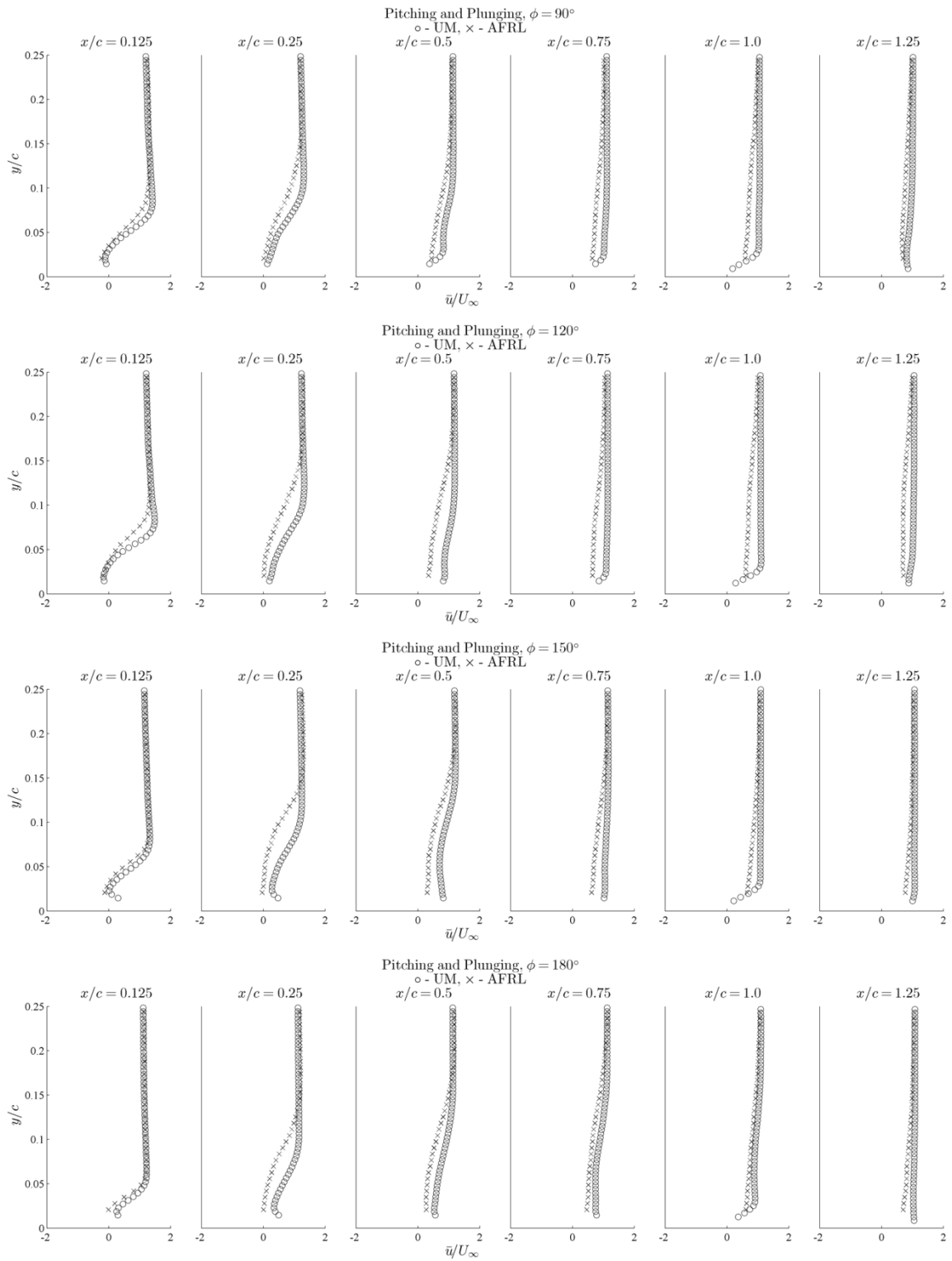
Figure 14. University of Michigan and AFRL pitching and plunging three-dimensional flat plates at $\phi = 90^\circ - 180^\circ$***, distributions of normalized*** $\bar{u}$ ***in the y-direction at selected chordwise stations (x/c = 0 corresponds to the leading edge)***
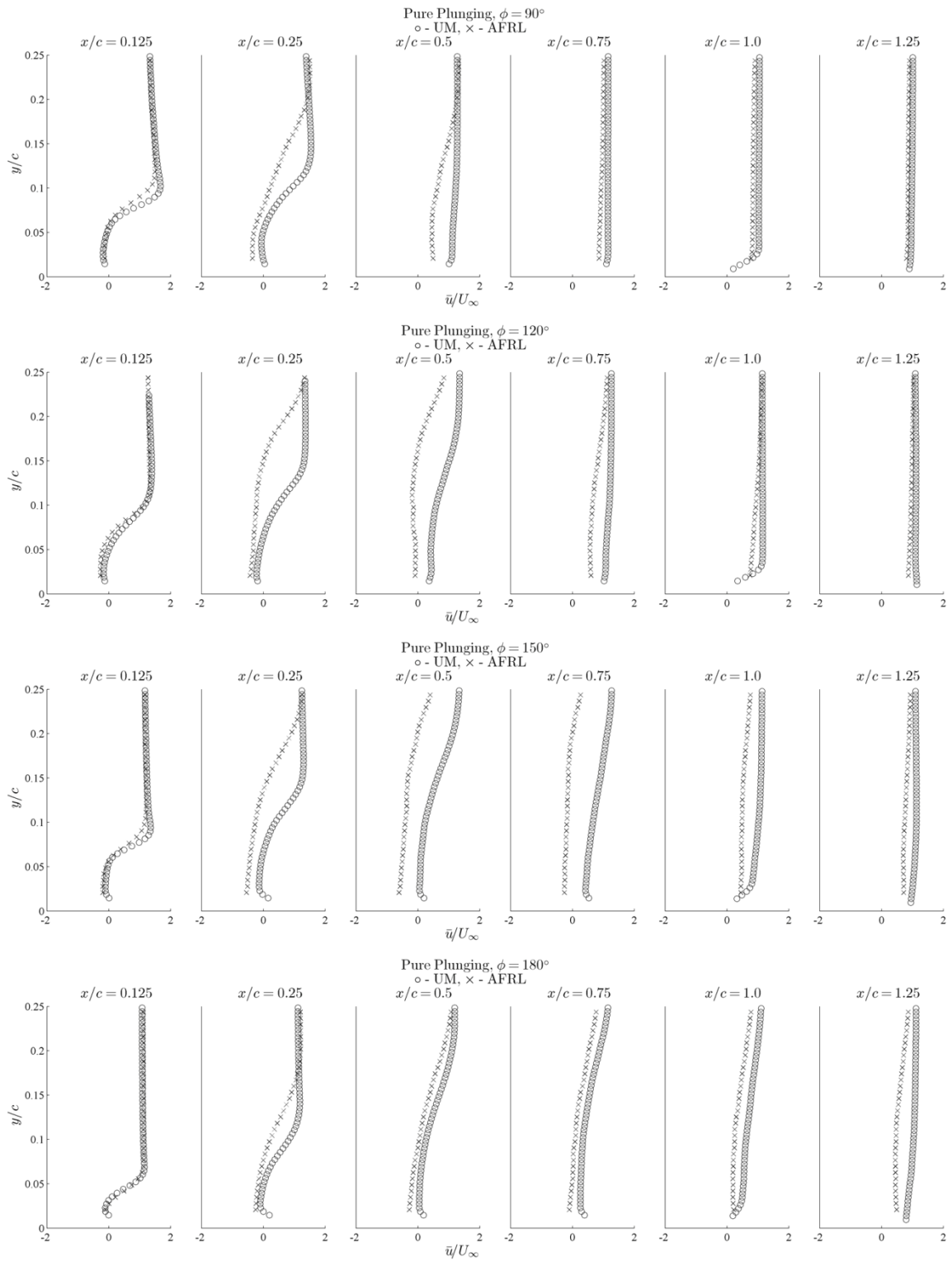
Figure 15. University of Michigan and AFRL plunging three-dimensional flat plates at $\phi = 90^\bullet - 180^\bullet$***, distributions of normalized*** $\bar{u}$ ***in the y-direction at selected chordwise stations (x/c = 0 corresponds to the leading edge)***

American Institute of Aeronautics and Astronautics

IV. Discussion

A. Re effect on two-dimensional flat plate

Re-independence was shown in Baik, *et al*[4]. for the pitching and plunging 2D flat plate, and similar reasoning suggested Re-independence for pure-plunge as well. Here we check the latter hypothesis.

Comparison of the contours of normalized $\bar{u}$ and ω in Figure 6 and Figure A.1 (repeated from Baik, *et al*[4]) provides a qualitative indication of Re dependence. The comparison of the contours shows a qualitative difference at $\phi = 120°$ and $150°$ in the interaction of the leading and trailing edge vortices. The Reynolds number 30,000 trailing edge vortex forms earlier than the Reynolds number 60,000 trailing edge vortex. For a more in depth analysis of this difference the normalized $\bar{u}$ distributions are plotted in Figure 16.

The normalized $\bar{u}$ distributions in Figure 16 are plotted at $\phi = 90° - 150°$. The observations of the normalized $\bar{u}$ and ω contours is confirmed by the distributions in Figure 16. At $\phi = 120°$ and $150°$ the chord locations near the trailing edge ($x/c = 75\%$ and 100%) show that the different trailing edge vortex formations have a significant effect on the normalized $\bar{u}$ distribution.
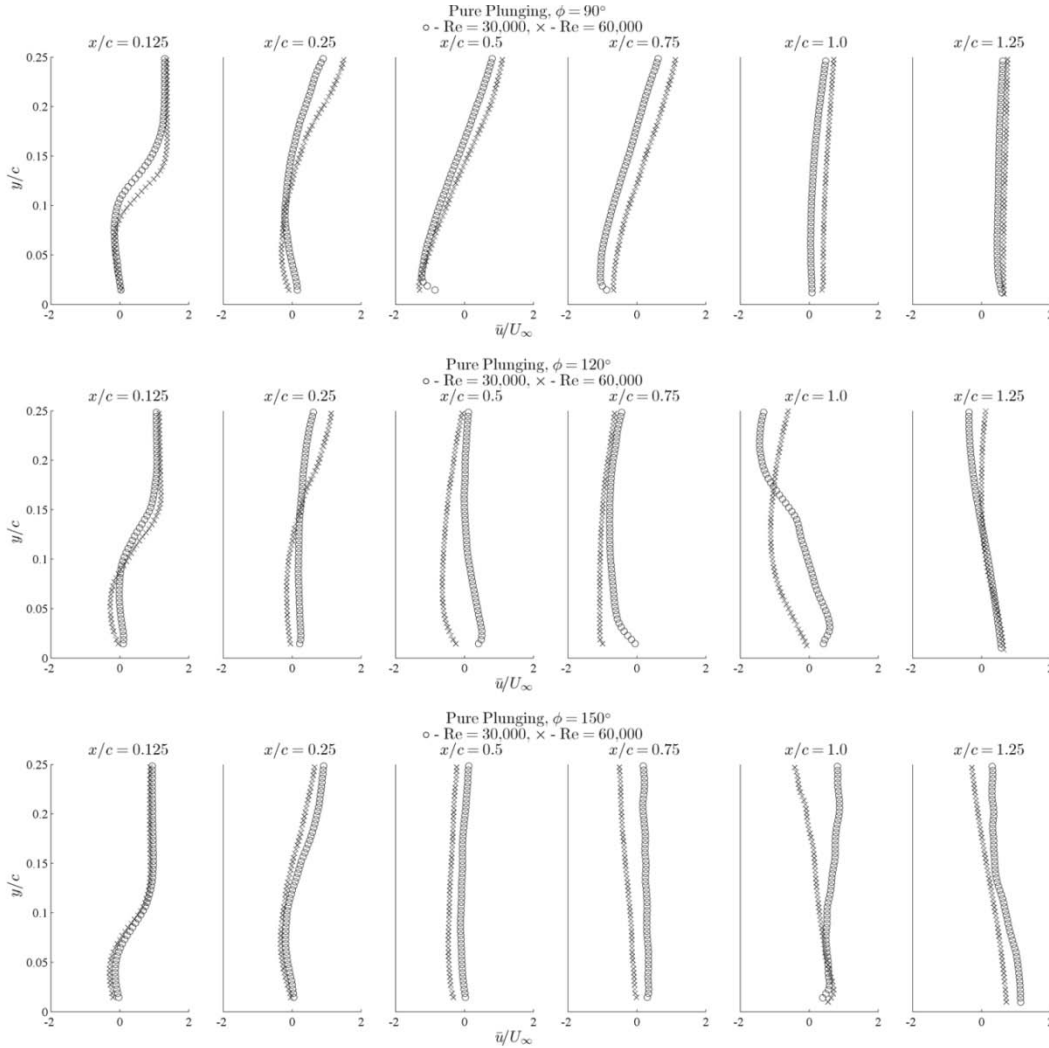

Figure 16. Reynolds number 30,000 and 60,000 for plunging motion at $\phi = 90° - 150°$, ***distributions of normalized $\bar{u}$ in the y-direction at selected chordwise stations (x/c = 0 corresponds to the leading edge)***

B. Aspect ratio effect on flow separation

The primary objective of the current work is to examine the difference between the 2D and 3D plates. In brief, this difference is the temporal evolution of the closed leading edge separation.

For the 2D plate in either motion, a closed leading edge separation grows towards the trailing edge during the downstroke, and . During the closed leading edge separation either forms a leading edge vortex that separates before the bottom of the downstroke, or the separation becomes open when the reattachment point reaches the trailing edge. Though a similar region of closed leading edge separation forms near the leading edge of the 3D plate, the region of closed separation does not significantly grow during the downstroke. Figure 17 illustrates the different temporal evolutions of the flow separation from $\phi = 90 - 150°$ for both plates.
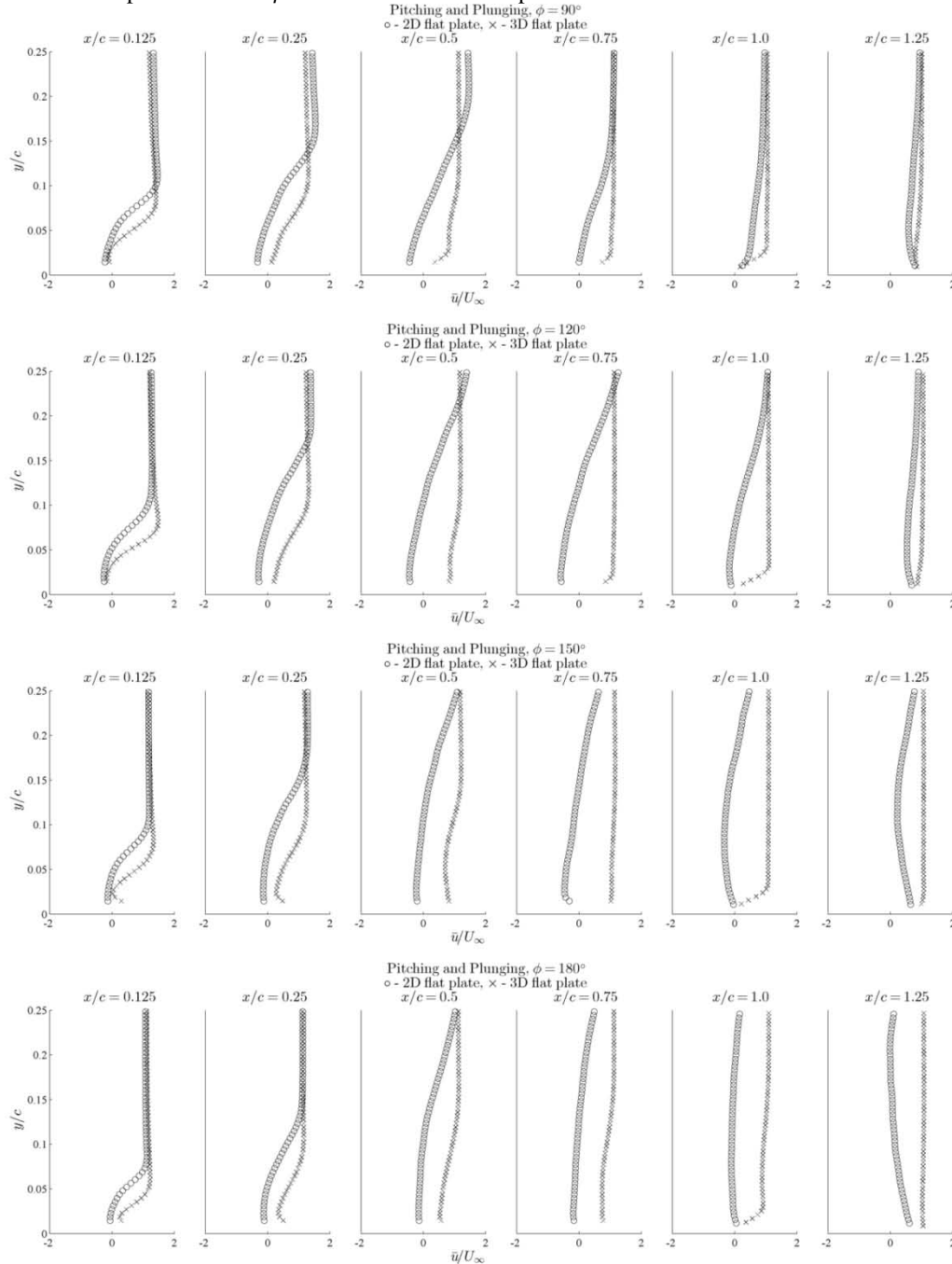

Figure 17. Pitching and plunging two- and three-dimensional flat plates at $\phi = 90° - 180°$, distributions of normalized $\bar{u}$ in the y-direction at selected chordwise stations (x/c = 0 corresponds to the leading edge)

American Institute of Aeronautics and Astronautics

For analyzing the normalized $\bar{u}$ distributions in Figure 17, we focus on the 50% and 75% chord locations, since this is the region of the flat plate where the reattachment point is evident.

At $\phi = 90°$, the difference between the two plates can already be seen at 50% and 75% chord. For the 2Dplate the growing separation is affecting these chord locations by reducing normalized $\bar{u}$ and the flow reattaches near the 75% chord location. The 3D flat plate remains relatively unaffected by comparison at the same chordwise location and the flow reattaches near the 25% chord location.

At $\phi = 120°$ the differences become significant at the 50% and 75% chord locations. At the 50% chord location the difference in normalized $\bar{u}$ near the flat plate's surface for the two- and three-dimensional flat plates is on the order of the freestream velocity. The flow over the two-dimensional flat plate reattaches near the trailing edge and the three-dimensional flat plate, again, reattaches near the 25% chord location.

At $\phi = 150°$ the separation region has an even greater influence on the 50% and 75% chord locations for the two-dimensional model. The two-dimensional model's normalized $\bar{u}$ distribution not only shows growth of the separated region in the x-direction but also in the y-direction. Similar to the previous two phases of motion the separation of three-dimensional model is limited to influencing the 0% and 25% chord locations.

To better quantify the differences between 2D and 3D plate flowfields, Figure 18 compares normalized $\bar{u}$ distributions at $\phi = 90° - 180°$.
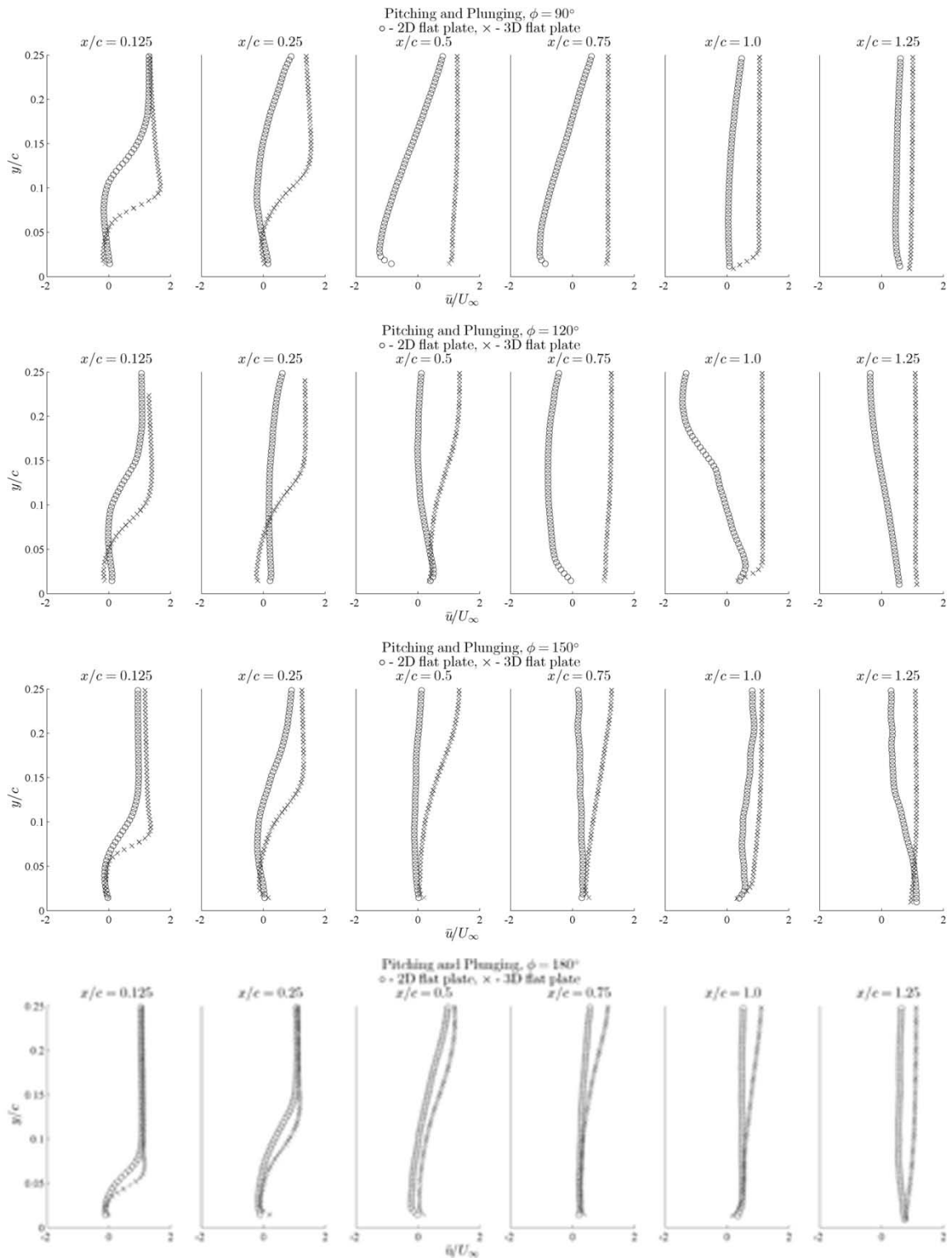
American Institute of Aeronautics and Astronautics

Figure 18. Plunging two- and three-dimensional flat plates at $\phi = 90^{\bullet} - 180^{\bullet}$, distributions of normalized $\bar{u}$ in the y-direction at selected chordwise stations (x/c = 0 corresponds to the leading edge)

The normalized $\bar{u}$ distributions for the two plates are not comparable before large leading and trailing edge vortices are shed in the two-dimensional case. This poor comparison is present from $\phi = 90° - 120°$. While the 2D plate's normalized $\bar{u}$ distributions are dynamically changing for these phases, the 3D plate's normalized $\bar{u}$

distributions are comparatively static. The 3D plate over these phases shows the closed leading edge separation that does not extend beyond the half-chord.

C. Extent of flow three-dimensionality

The three-dimensionality of the flow over the both flat plates was investigated with flow visualization in the crossflow plane.

Dye streaks for the 2D plate showed minimal deviations from the plane of the injector rake. , but 3D plate results showed significant deviations from the plane of the injector. For the same phases of motion as the PIV, flow visualization of the spanwise flow is shown in Figure 19 for the pitching-and-plunging and pure-plunging 3D flat plate.
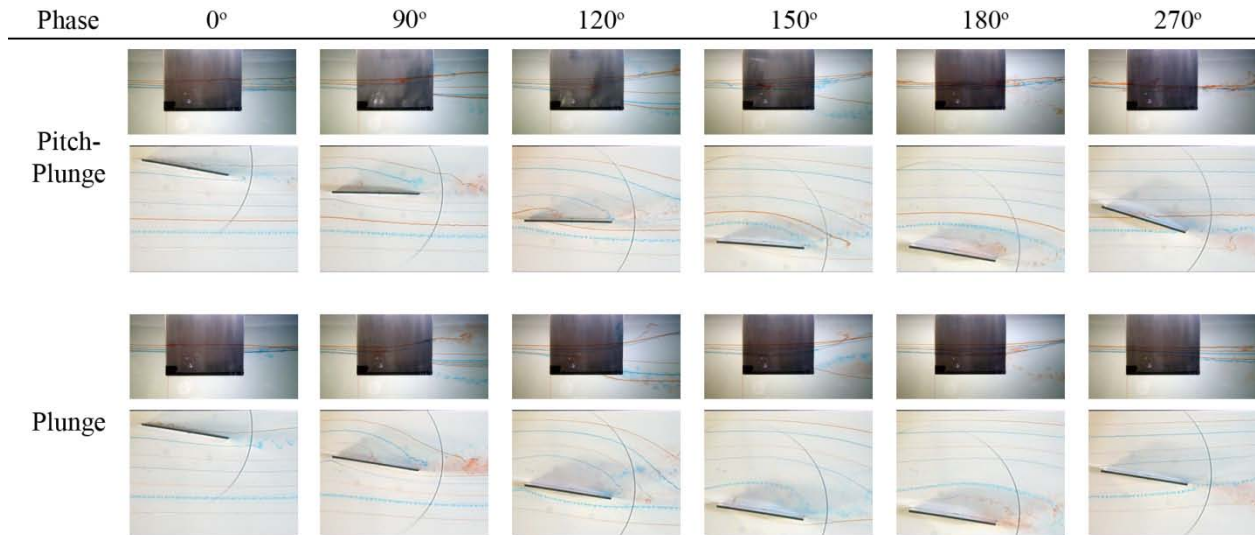

Figure 19. Flow visualization showing the spanwise flow for the 3D model in pitch-plunge and pure plunge. Notable spanwise flow occurs at the same range of phases for both motions, 90-180 degrees. Flow is from left-to-right and the camera views the suction side of the flat plate.

The pitching and plunging 3D plate shows significant spanwise flow from $\phi = 90° - 180°$. The most significant three-dimensionality is caused by the rollup of the wing tip vortex. At $\phi = 120°$ and $150°$ the wing tip vortex entrainment of dye from the pressure side of the flat plate can clearly be noted in Figure 19.

The plunging 3D plate has even significant spanwise flow associated with a wing tip vortex from $\phi = 90° - 180°$. The wing tip vortex for the plunge motion causes more three-dimensionality at than the pitch-plunge motion. This is an excepted result since the large effective angle of attack time history for the plunge motion will cause a larger pressure differential between the pressure and suction side of the flat plate., as expected given the higher effective angle of attack at the plunge downstroke.

Significant three-dimensional flow was not observed in the closed leading edge separation, other than a gradual inboard deflection of the dye streaks.

V. Conclusions

To generalize earlier work on wall-to-wall plunging and pitching-plunging plates to a plate of aspect ratio 2, experiments at the University of Michigan's low-turbulence water tunnel used dye flow visualization in streamwise and crossflow planes, and particle image velocimetry in streamwise planes. Findings can be summarized as follows:

- For both the 2D and 3D plates, a region of closed leading edge separation is present at $\phi = 90°$, halfway down the downstroke. For the 2D flat plate after $\phi = 90°$ the region of closed separation either forms a large leading edge vortex that sheds prior to the bottom of the downstroke (plunge) or the bottom of the downstroke is reached and the reduced effective angle of attack causes flow reattachment (pitch-plunge). For the 3D plate after $\phi = 90°$ the region of closed separation remains closed and confined to a reagion bounded by the leading edge and the half-chord.

- A discernable Reynolds number effect is present for the 2D plates in pure-plunge motion when comparing the Reynolds number 30,000 and 60,000. The pure-plunge motion makes a significantly larger excursion in effective angle of attack from the static stall angle of attack compared to the pitch-plunge motion, resulting in a large leading edge vortex that forms and convects downstream. Presumably, this Reynolds number effect is absent in the pitch-plunge motion because the different flow physics associated with the large leading and trailing edge vortices created by the pure-plunge motion.

- The magnitude and physical extent of second order turbulence statistics for the low aspect ratio model are significantly smaller than the nominally 2D model

- Spanwise flow was observed by dye flow visualization for the 3D plate, but not for the 2D plate, thus providing confirmation for assumption of 2D flow for the latter. Spanwise flow for the 3D plate is associable with interaction with the wing tip vortex for both pitch-plunge and plunge motions. No appreciable spanwise flow was found in the closed leading edge separation.

- The University of Michigan and the AFRL PIV while qualitatively similar showed a greater chordwise separation for the AFRL PIV than the University of Michigan. Both data sets have closed separation through the downstroke with the exception being the plunging ARLF PIV at $\phi = 180°$ where open separation is observed. Without force measurement the significance of the flowfield differences cannot be assessed.

Appendix

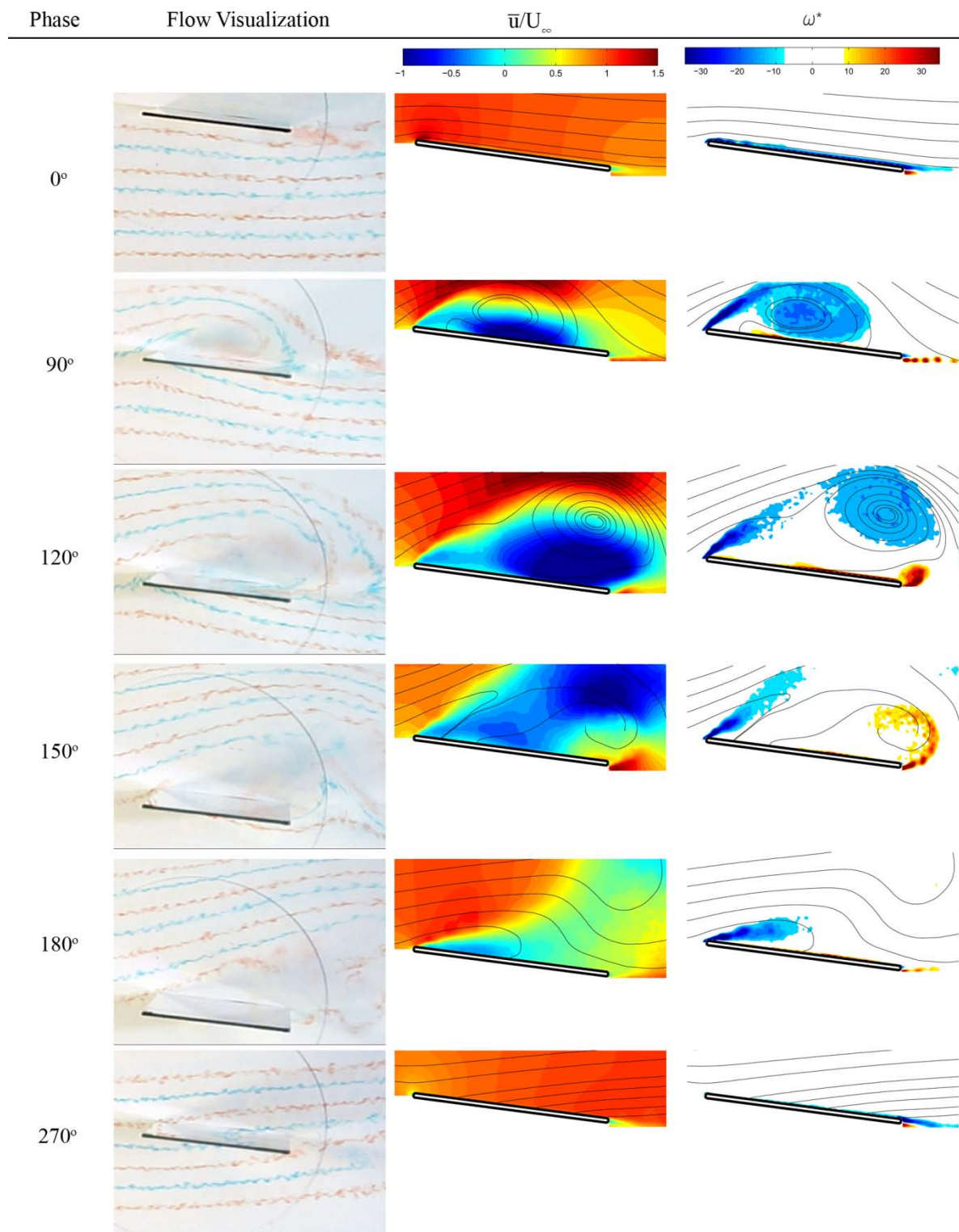## A. Flow visualization and PIV from Baik, *et al.*[4]

Figure A.1. Flow visualization, ū, and ω for the plunging 2D flat plate at Re = 60,000 (Baik, et al.[4])*

Acknowledgements

References

[1] Shyy, W., Lian, Y., Tang, J., Viieru, D., & Liu, H. (2008). *Aerodynamics of Low Reynolds Number Flyers*. Cambridge University Press.

[2] Ol, M., Bernal, L., Kang, C., and Shyy, W., "Shallow and deep dynamic stall for flapping low Reynolds number airfoils," *Experiments in Fluids*, Vol. 46, Nr. 5, 2009, pp. 883-901

[3] McCroskey, W.J, Carr, L.W., and McAlister, K.W., "Dynamic stall experiments on oscillating airfoils," *Journal of Aircraft*, Vol. 14, Nr. 1, 1976, pp. 57-63

[4] Baik, Y., Rausch, J.M., Bernal, L.P., and Ol, M.V., "Experimental Investigation of Pitching and Plunging Airfoils at Reynolds Number between 1x10^4 and 6x10^4," AIAA 2009-4030.

[5] Anderson, J. M., K. Streitlien, D. S. Barrett, and M. S. Triantafyllou. "Oscillating Foils of High Propulsive Efficiency." *Journal of Fluid Mechanics* 360 (1998): 41-72.

[6] Kang, C-K., Baik, Y.S., Bernal, L.P., Ol, M.V., and Shyy, W. "Fluid Dynamics of Pitching and Plunging Airfoils of Renolds Number between 1x10^4 and 6x10^4." *47th Aerospace Sciences Meeting*. Orlando: AIAA, 2009.

American Institute of Aeronautics and Astronautics